Journal of Electronic Materials (2023) 52:6537–6550
https://doi.org/10.1007/s11664-023-10443-5

ORIGINAL RESEARCH ARTICLE

Enhanced Thermoelectric Performance of a HfS_2 Bilayer by Strain Engineering

Hao Wang[1] · **Juan Xiang**[1] · **Bo Dai**[1] · **Ni-Na Ge**[1] · **Xiao-Wei Zhang**[1] · **Guang-Fu Ji**[2]

Received: 18 September 2022 / Accepted: 4 April 2023 / Published online: 19 July 2023

Abstract

For two-dimensional transition metal dichalcogenides, the thermoelectric properties of the material are affected by layer thickness and lattice strain. In this paper, we investigate the thermoelectric properties of a HfS_2 bilayer under different biaxial tensile strains by first-principles calculations combined with Boltzmann equations. The presence of degenerate bands in the HfS_2 bilayer and the absence of its monolayer results in the better thermoelectric performance of the HfS_2 bilayer than its monolayer. Moreover, this strain increases the band degeneracy of the HfS_2 bilayer even more, and the degenerate bands and stepped 2D density of states lead to a high power factor. In addition, the lattice strain increases the phonon scattering rate and reduces the phonon lifetime of the HfS_2 bilayer, resulting in a decrease in the lattice thermal conductivity. Ultimately, we obtained a maximum *ZT* value of 1.76 for the unstrained HfS_2 bilayer at the optimal doping concentration. At this time, its power factor and thermal conductivity are 53.01 mW/mK^2 and 9.06 W/mK, respectively. When the strain reaches 3%, for the *n*-type doped HfS_2 bilayer, the power factor and thermal conductivity are 69.87 mW/mK^2 and 6.36 W/mK, respectively, and the maximum *ZT* value is 3.29. For the *p*-type doped HfS_2 bilayer, the maximum *ZT* value appears at 6% strain, which is 1.83, at which the power factor and thermal conductivity are 13.81 mW/mK^2 and 2.27 W/mK, respectively.

Keywords Thermoelectric properties · lattice strain · first-principles calculations · HfS_2 bilayer · *ZT* value

Introduction

As a typical two-dimensional (2D) layered material, transition metal dichalcogenides (TMDCs)[1–3] are promising high-performance thermoelectric materials due to their high electrical conductivity and low thermal conductivity, which are mainly used in the fabrication of wearable heating/cooling devices and thermoelectric generators. Moreover, TMDCs have received extensive attention in recent decades[4–6] due to semiconducting properties and possess excellent mechanical properties, physical properties and chemical stability.

Increasing the thermoelectric efficiency of TMDC materials has been an ambitious goal for decades. It is found that there are many factors affecting the properties of thermoelectric materials, such as the structure, number of layers and external stress. There are two main stable structures of TMDCs at room temperature. One is the 2H phase with a triangular prism coordination structure with the space group $P\bar{6}m2$, and the other is the 1T phase with an octahedral coordination structure, with space group $P\bar{3}m1$. The most common TMDC materials with the 2H phase structure are MoS_2, $MoSe_2$, WS_2 and WSe_2, and the materials with 1T phase

---

Hao Wang and Juan Xiang have contributed equally to this work.

✉ Ni-Na Ge
genina911@163.com

Hao Wang
wh249370345@163.com

Juan Xiang
jxiang_165@163.com

Bo Dai
daibo@swust.edu.cn

Xiao-Wei Zhang
xiaoweizhang@swust.edu.cn

Guang-Fu Ji
cyfjkf@126.com

[1] State Key Laboratory of Environment-Friendly Energy Materials, Southwest University of Science and Technology, Mianyang 621010, People's Republic of China

[2] Laboratory for Shock Wave and Detonation Physics Research, Institute of Fluid Physics, Chinese Academy of Engineering Physics, Mianyang 621900, China

structure are HfS_2, $HfSe_2$, ZrS_2 and $ZrSe_2$. By comparing the band structure of the 1T and the 2H phase structure, it can be found that the band gap of the 1T phase structure is generally smaller and the 2H phase is larger.[7,8] It is well known that a large band gap is not conducive to optimizing the thermoelectric properties of materials, because a large amount of doping is required to achieve the best performance of the material, and a large band gap usually means a lower carrier concentration. Meanwhile, a larger band gap may mean a larger Seebeck coefficient, but also a smaller conductivity, which may ultimately lead to a smaller power factor and poorer thermoelectric performance. Yumnam et al. recently confirmed that the lattice thermal conductivity of Zr- and Hf-based bulk TMDCs is lower than that of Mo- and W-based bulk TMDCs due to the strong coupling of low-frequency optical and acoustic modes.[9] For instance, the lattice thermal conductivity of ZrS_2 monolayer is only 3.29 W/mK at 300 K.[10] But the lattice thermal conductivities of MoS_2 and WSe_2 monolayers are as high as 100 W/mK and 40 W/mK.[8,11] Likewise, the lattice thermal conductivities of $ZrSe_2$ and $HfSe_2$ monolayers are 1.2 W/mK and 1.8 W/mK at 300 K.[7] This may indicate that the thermoelectric performance of the 1T phase structure is better than that of the 2H phase structure in TMDCs.

With the development of fabrication technology, monolayer, bilayer and few-layer 2D materials can be successfully prepared. Recent studies on TMDCs have shown that the thermoelectric properties of 2D materials with different layer thicknesses will be different.[3,12] Wickramaratne et al. reported that the thermoelectric properties of most MoS_2, $MoSe_2$, WS_2 and WSe_2 with bilayer structures are better than other few-layer structures and bulk structures.[12] The band structure and density of states of 2D TMDCs change when increasing from monolayer to multilayer due to the interlayer coupling effect. The Seebeck coefficient of monolayer MoS_2 is 2055.4 μV/K, while the *S* of its bilayer structure increases to 2344.9 μV/K.[13] Meanwhile, the work by Wickramaratne et al. also showed that the power factors of an *n*-type doped MoS_2 monolayer and WS_2 monolayer are 0.13 W/mK^2 and 0.24 W/mK^2 at 300 K, and the power factors increase to 0.14 W/mK^2 and 0.28 W/mK^2 as the monolayer increases to a bilayer.[12] Finally, the maximum ZT value of MoS2 increased from 0.967 (monolayer) to 0.974 (bilayer),[13] and the maximum ZT value of MoS2 increased from 1.52 (monolayer) to 1.98 (bilayer).[12] Yun et al.[14] and Goyal et al.[15] demonstrate that the thermoelectric characteristics of Bi_2Te_3 and Bi_2Se_3 increase with decreasing thickness, which is due to an increase in ZT produced by the form of the density of states, which enhances the power factor. Moreover, the bilayer BP has substantially lower lattice thermal conductivity than the monolayer 300 W/mK, which is roughly 24 W/mK, as a result of the van der Waals (vdW) interaction. As a result, at 1200 K, the BP bilayer obtains an outstanding ZT of around 1.8.[16] Hence, thermoelectric properties are significantly influenced by weak coupling contact. However, the current studies on the thermoelectric properties of TMDCs focus on the 2H phase structure and lack the research on the thermoelectric properties of the 1T phase structure.

Furthermore, tensile strain has been found to also affect the thermoelectric properties of 2D TMDCs. Tseng et al.[17] found that applying tensile strain to $TiSe_2$ monolayer and $HfSe_2$ monolayer changed the band structure and tuned band degeneracy and induced changes in electron transport properties. As the tensile strain increased from 0% to 8%, the power factors[17] of $TiSe_2$ monolayer and $HfSe_2$ monolayer increased from 2.92 W/mK^2 and 1.45 W/mK^2 to 3.40 W/mK^2 and 2.80 W/mK^2, respectively. Finally, the *ZT* values of $TiSe_2$ monolayer and $HfSe_2$ monolayer are increased from 0.15 and 1.19 to 1.64 and 1.99[17] through the tensile strain. Similar results are obtained by Qin et al.[18] by applying tensile strain to a $ZrSe_2$ monolayer. As the tensile strain increased from 0% to 7.5%, the maximum *ZT* values for *p*-type and *n*-type doping increase from 2.13 and 4.26 to 3.84 and 4.58,[18] respectively.

Hf-based materials of transition metal dichalcogenides generally have lower lattice thermal conductivity due to the heavier Hf atom and the coupling between the acoustic branch and the low-frequency optical branch,[7,19] which is advantageous for obtaining high thermoelectric performance.[20–22] Studies have demonstrated that HfS_2 has a high carrier mobility compared to other two-dimensional semiconductor materials (such MX_2 (M = Mo, W, Sn; X = S, Se) of other transition metal dichalcogenides).[23] This suggests that it has outstanding electrical transport capabilities, which results in a high power factor. Secondly, HfS_2 has low thermal conductivity. Owing to its excellent characteristics, it has good thermal conductivity among many materials of MX_2 (M = Cr, Mo, W, Ti, Zr, Hf; X = O, S, Se, Te). In summary, as our research object, HfS_2 has excellent thermoelectric properties among many materials.[9,20,24]

Recently, based on the successful preparation of few-layer HfS_2 by Wang et al.[2] and combined with the findings of Wickramaratne et al.,[12] we chose to study the thermoelectric properties of HfS_2 bilayers in this paper. In pursuit of higher thermoelectric properties, we subjected the HfS_2 bilayer to biaxial tensile strain and calculated its *ZT* value.

Computational Methods

Based on density functional theory, we use the generalized gradient approximation (GGA) within Perdew–Burke–Ernzerhof (PBE) formulation exchange–correlation interaction to optimize the HfS_2 bilayer in the Vienna Ab initio Simulation Package (VASP).[25–27] In addition, to avoid the influence of interlayer force, Grimme's

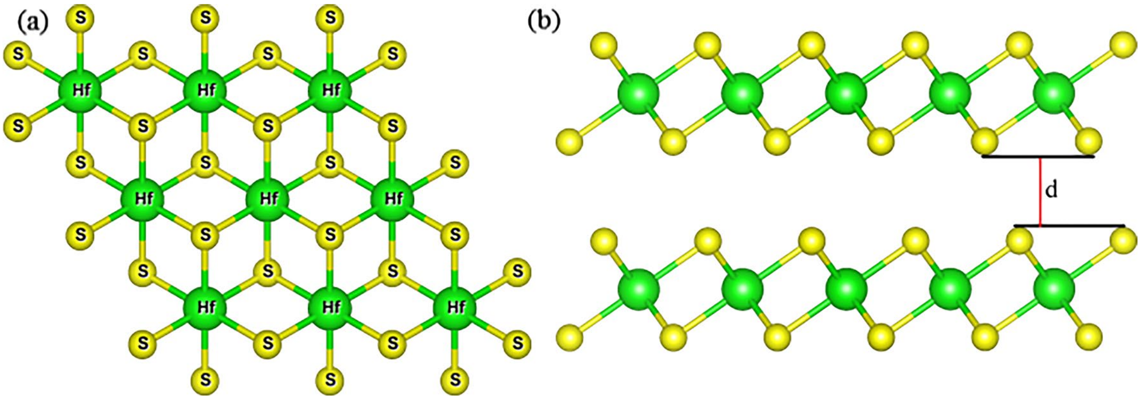

Fig. 1 (a) Top and (b) side views of HfS$_2$ bilayer.

Table I Comparison of the lattice constants of the HfS$_2$ bilayer calculated in this paper with the lattice constants (Å) of bulk and monolayer HfS$_2$ in the literature

	Method	Lattice constant (Å)
	Experiment (bulk)	3.631[38]
HfS$_2$ monolayer	PBE	3.65[39]
HfS$_2$ monolayer	PBEsol	3.64[4]
HfS$_2$ bilayer	HSE06	3.616 (present)

DFT-D3 method is used to carry out van der Waals (vdW) correction for the calculation method.[28] The plane-wave energy cutoff is chosen as 600 eV for the HfS$_2$ bilayer, and the Monkhorst–Pack k mesh is $21\times21\times1$. Geometrical structures were relaxed until the force on each atom was less than 0.001 eV Å^{-1}. In order to avoid the interaction with periodic images, a 26 Å thickness of vacuum slab is added in the direction of the vertical 2D plane for HfS$_2$ bilayer. In the subsequent calculation of the band structure and electron transport properties, the Heyd–Scuseria–Ernzerhof (HSE) screened nonlocal exchange functional of the generalized Kohn–Sham scheme was used to correct the results.[29]

Thermoelectric transport properties including Seebeck coefficients (S) and the electrical conductivity over relaxation time (σ/τ) are calculated by using the electron Boltzmann transport theory within relaxation time approximation (RTA) as implemented in the BoltzTrap software package.[30] A large $51\times51\times1$ k-point Monkhorst–Pack grid was used in the calculation of the band energies, resulting in the final transport properties. Finally, the relaxation time (τ) is estimated by using Bardeen–Shockley deformation potential theory based on the effective mass approximation:

$$\tau = \frac{\mu m^*}{e}, \tag{1}$$

$$\mu = \frac{e\hbar^3 C_{2d}}{k_B T m^* m_d E_1^2}, \tag{2}$$

where μ, C_{2D}, and E_l are the carrier mobility, the effective elastic modulus and the deformation potential constant, respectively, and $m^* = \hbar^2\left[\partial^2 E/\partial k^2\right]^{-1}$ is the effective mass of the carrier, and $m_d = \sqrt{m_x^* m_y^*}$ is the average effective mass.[31,32] The electronic thermal conductivity was calculated by the Wiedemann–Franz law:

$$\kappa_e = L\sigma T, \tag{3}$$

where L is the Lorenz number, and we obtain a sufficiently accurate value through a simple equation:[33]

$$L = 1.5 + \exp\left[-|S|/116\right] \tag{4}$$

where S is the Seebeck coefficient in μV/K and L is in 10^{-8} WΩK^{-2}.

The lattice thermal transport was obtained by solved the phonon Boltzmann transport equation as implemented in ShengBTE.[34] The phonon dispersion and second-order interatomic force constants (IFCs) were obtained by using the finite displacement method as implemented in the PHONOPY code from a $3\times3\times1$ supercell with $5\times5\times1$ k-point Monkhorst–Pack grid based on the relaxed unit cell.[35] The third-order force constants were calculated and extracted using the same supercell and k mesh as the second-order force constants. The formula of κ_l can be expressed as:

$$\kappa_{\alpha\beta} = \frac{1}{\mathrm{SH}}\sum_{\lambda} C_\lambda v_{\lambda\alpha} v_{\lambda\beta}\tau_\lambda \tag{5}$$

in which S is the surface area, H is determined by $H_{\mathrm{HfS_2}} = 2(h_{\mathrm{HfS_2}} + r_{\mathrm{S}}) + d$ for HfS$_2$ bilayer, where h_{HfS_2} is the height difference of the top S and the bottom S atom and d,

r_S is the distance between the two layers and van der Waals radii of the S atom.[36,37]

Results and Discussion

Lattice Parameters and Structural Stability

First, we obtained the geometry and lattice parameters of the HfS_2 bilayer by lattice optimization. The top and side views of the HfS_2 bilayer structure are shown in Fig. 1, where *d* means the distance between the two layers. As shown in Table I, the lattice constant of the HfS_2 bilayer is 3.616 Å and the *d* is 3.006 Å. This lattice constant is in good agreement with the values reported in previous literature.[4,38,39] As shown in Fig. S1 of the supplemental material, we ran ab initio molecular dynamics (AIMD) simulations of the bilayer HfS_2. Given that it maintains its stability at high temperatures beyond 10 ps, bilayer HfS_2 is expected to mature into a medium- to high-temperature thermoelectric material.

Based on the above optimized structure, we applied a series of in-plane biaxial tensile strains to the HfS_2 bilayer, defining the strain degree as

$$\varepsilon = \left(a - a_0\right)/a_0 \times 100\% \tag{6}$$

where a_0 and a denote the unstrained cell parameter and the strained cell parameter.

Biaxial tensile strains from 0 to 7% are considered. We calculated the phonon dispersion curve to verify the structural stability of the HfS_2 bilayer in the range of 0–7% strain. As shown in Fig. 2, the phonon dispersion curve has no imaginary frequency, which means the structure is stable.

Electronic Transport Properties

In order to analyze the effect of strain on the electronic band structure of the HfS_2 bilayer, the electronic band structures, total density of states and partial density of states of the Brillouin zone along the K–Γ–M–K path are calculated based on the HSE06 method, as shown in Fig. 3, and the HfS_2 bilayer at strains from 0% to 7% behaves as an indirect-band-gap semiconductor. The conduction band minimum (CBM) and valence band maximum (VBM) of the unstrained HfS_2 bilayer are located at the high symmetry point M point and Γ point, respectively, while at the Γ point, an obvious valley degeneracy that does not exist in the HfS_2 monolayer is found. In addition, splitting of the band is also found at the M point, and the energy difference between the two conduction band valleys is about 0.07 eV. According to the research, when the energy difference between the band valley is less than a certain value (compared with k_BT, where k_B is the Boltzmann constant), it can be considered to achieve an effective degeneracy,[15,40–42] and the thermoelectric properties of the material are affected.[15,41,43] Moreover, the band gap gradually increases with the increase of strain. The band gap is 1.92 eV at 0% strain and the band gap is 2.37 eV at 7% strain. At 3% strain, the VBM moves from the high symmetry point Γ to between K and Γ, and the valence band top shifts again to the left in the Brillouin zone as the strain increases to 5%. Finally, the band structures are calculated in order to reveal the effect of the energy difference between the band valleys on the thermoelectric performance, as shown in Fig. 3a, where I and II denote the conduction band valley near the Fermi level (0 eV), and III, IV and V represent the valley of the valence band near the Fermi level, respectively. Furthermore, the energy difference between band valleys I and II (III and IV) is expressed as ΔC (ΔV), namely $\Delta C = E_\Gamma – E_{II}$, $\Delta V = E_{IV} – E_{III}$, and the relationship of ΔC and ΔV as a function of strain is shown in Fig. 4. ΔC decreases gradually with the increase of strain, while ΔV first decreases and then increases, and when the strain reaches 3%, ΔV reaches the minimum value of −0.017 eV. Therefore, the valleys of the valence band at III, IV and V are degenerate and the degeneracy is maximum at 3% strain. ΔV becomes larger as the strain increases from 3% to 5%, but as the strain continues to increase to 6% and 7%, ΔV tends to decrease again. But at the same time, it can be found that when the strain increases to 5%, the band structure at Γ begins to split, and as the strain continues to increase, the splitting degree increases. Therefore, when the strain increases from 5% to 7%, ΔV still decreases, but the band degeneracy decreases.

Such a trend can also be seen from the variation function of the electronic density of states with strain, as shown in Fig. 5. We can find that the valence band of the HfS_2 bilayer is mainly contributed by the *d* orbital of the Hf atom, while the conduction band is contributed by the *p* orbital of the S atom. When the strain reaches 3%, the slope of the electron total density of states (TDOS) at the VBM also reaches a maximum, which is due to the maximum degeneracy at the VBM. The slope of TDOS at the CBM increases gradually with the strain, and the slope of TDOS reaches the maximum at 7% strain. A larger slope of the density of states means a higher Seebeck coefficient (S).[44]

Next, the electrical transport properties of the HfS_2 bilayer under different strains and obtained τ by deformation potential theory (DP) are calculated (as shown in Table II). Ultimately, the relationship between the S, electrical conductivity (σ), power factor (PF) and the electronic thermal conductivity (κ_e) with the carrier concentration under different strains are obtained as shown in Fig. 6. As shown in Fig. 6a, the bilayer HfS_2 Seebeck coefficient increases as the degree of strain increases for *p*-type, and after peaking at 3% strain, the Seebeck coefficient begins to decrease with increasing strain. The difference is that the S of *n*-type doping increases

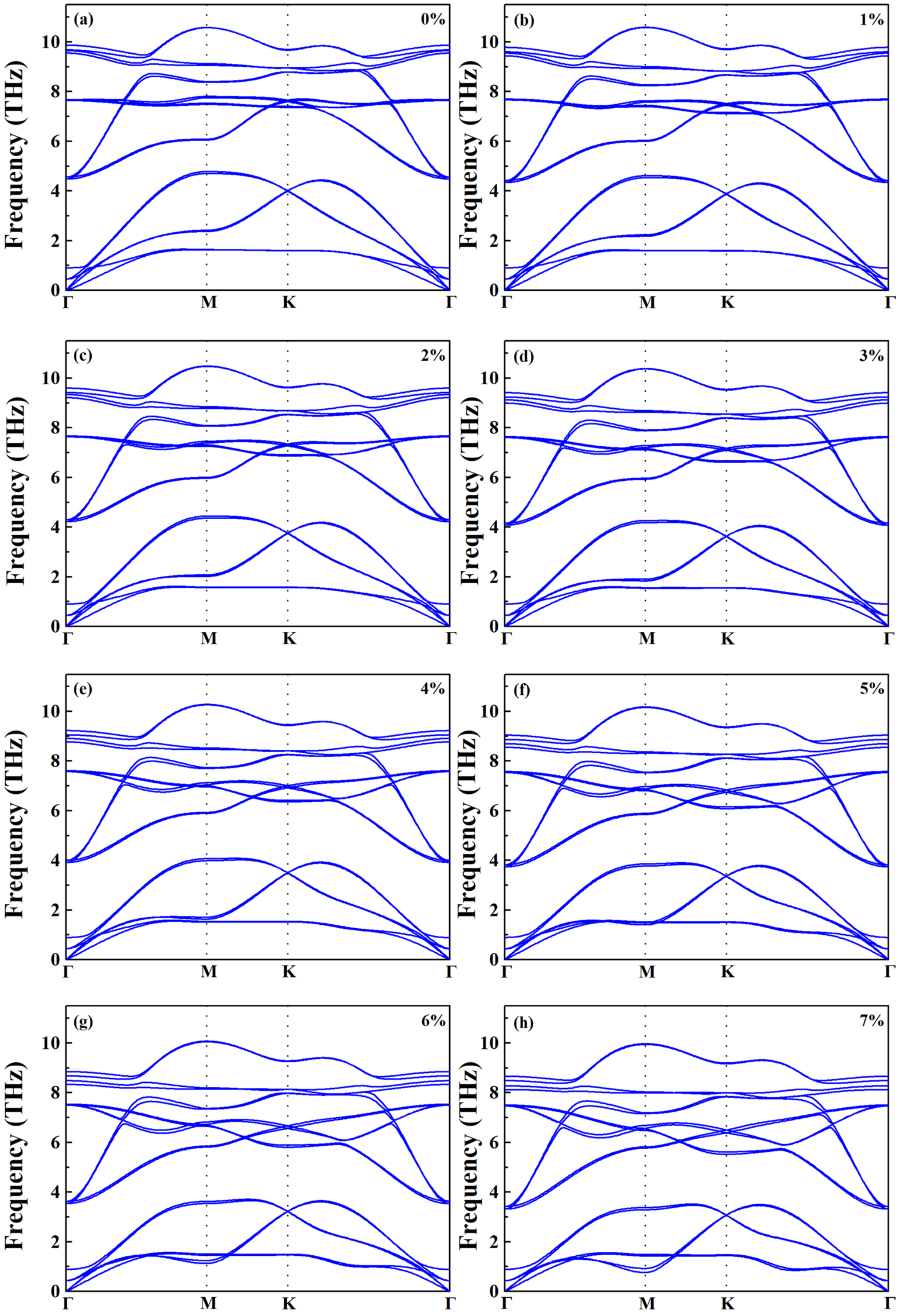

Fig. 2 The calculated phonon spectra of the HfS$_2$ bilayer under different biaxial strains, (a) 0%, (b) 1%, (c) 2%, (d) 3%, (e) 4%, (f) 5%, (g) 6%, (h) 7%.

gradually with strain, and the S is maximum at 7% strain. We can find that the change of the *S* is consistent with the change trend of the slope of the TDOS, which also shows that the improvement of the band degeneracy can effectively increase *S*. It can be seen from Fig. 6b that the σ of *n*-type doping is generally higher than that of *p*-type doping. However, the

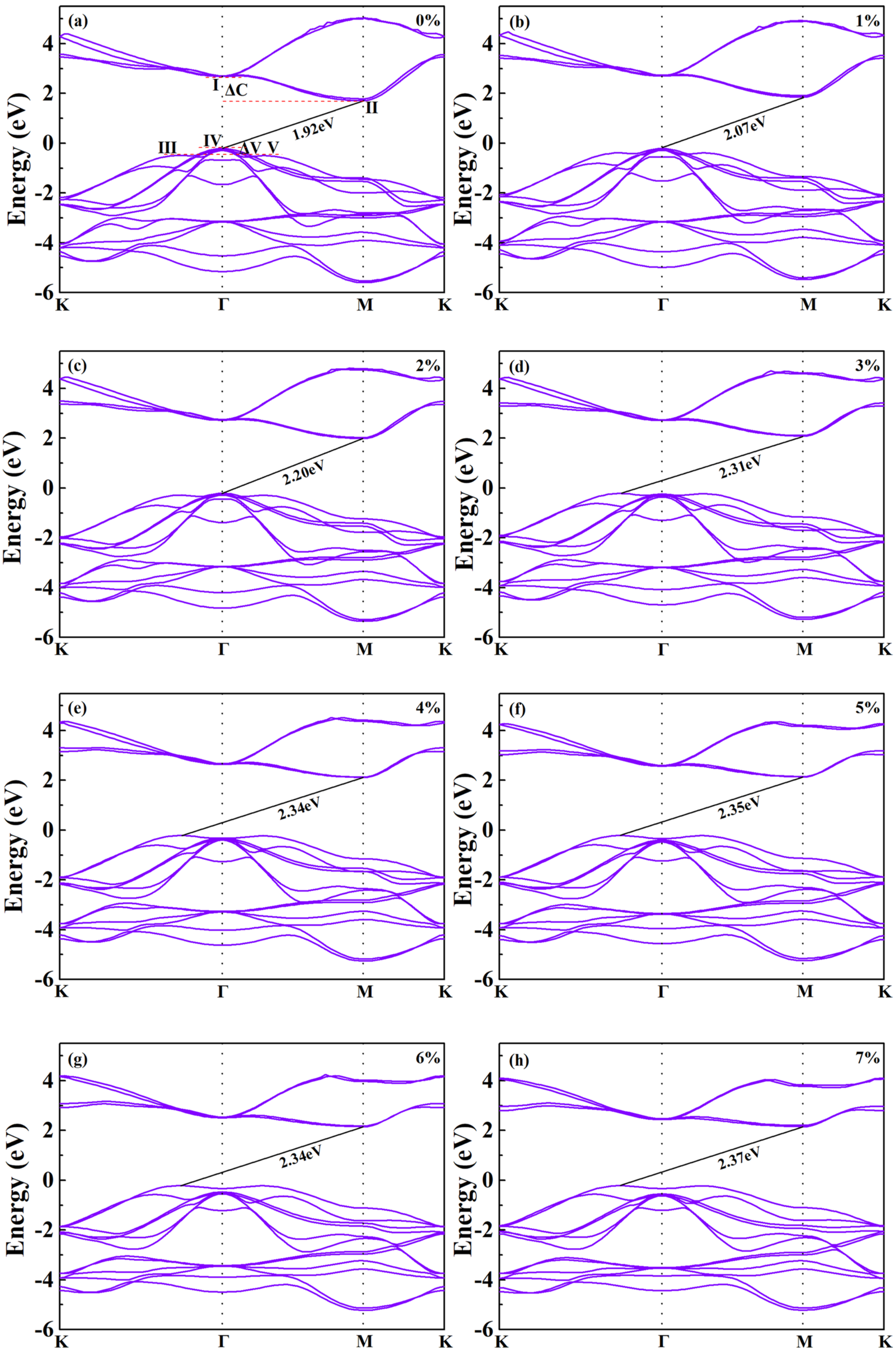

Fig. 3 The band structure of HfS_2 bilayer under different biaxial strain, (a) 0%, (b) 1%, (c) 2%, (d) 3%, (e) 4%, (f) 5%, (g) 6%, (h) 7%. The two conduction band valleys near the Fermi level (0 eV) are denoted by I and II, respectively. The three valence band valleys near the Fermi level are denoted by III, IV and V, respectively. ΔC (ΔV) represents the energy difference between I and II (III and IV).

σ of n-type doping is smaller than that of p-type when the strain is below 3% at low doping concentrations. The smaller σ of n-type doping is due to the larger electron effective mass and lower carrier mobility.

An evaluation of the thermoelectric performance of a material does not unilaterally consider the S or the σ, but the PF obtained by coupling S and σ. The biaxial strain affects the Seebeck coefficient and conductivity of the bilayer HfS_2, as shown in Fig. 6c, but it also significantly alters PF. For the p-type, the S of the p-type is higher than the n-type when the strain is more significant than 3%; however, the PF of the n-type is greater than the p-type due to the high σ. Moreover, for p-type HfS_2 bilayers, taking high carrier concentration as an example, PF reaches the peak of roughly 40 mW/mK^2 at 2%, while 3% PF is also relatively high. The pattern for PF is similar to that of S in that it increases initially before declining. For the n-type, although S gradually increases with strain, σ also presents a decreasing trend. The PF of the HfS_2 bilayer increases first and then decreases and reaches the peak at 3%, about 130 mW/mK^2, which is about 1.3 times higher than 0% (98 mW/mK^2). In addition, it is worth mentioning that when the strain is applied beyond a particular limit, PF will be smaller than the unstrained case, which is related to the mutual balance between the increased S and the decreased σ. This shows that optimizing the power factor of the HfS_2 bilayer does not require maximizing either S or σ, but rather both achieve appropriate values.

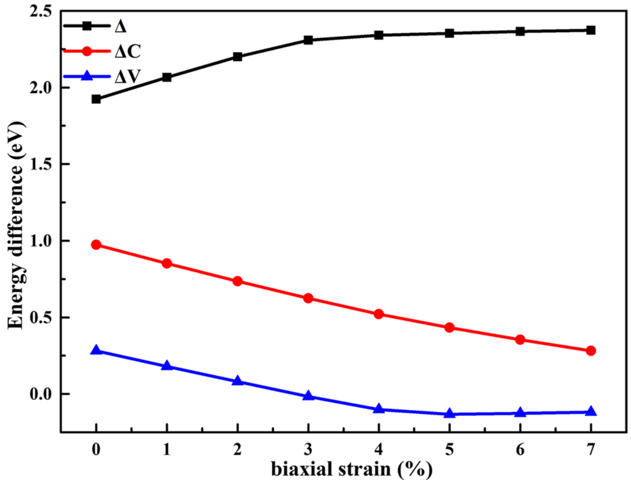

Fig. 4 Band gap (Δ) and energy difference between the conduction and valance band valleys (ΔC and ΔV) as a function of the applied biaxial strain.

Thermal Transport Properties

In this section, we discuss the effect of strain on thermal conductivity (κ). First, in order to obtain a more accurate κ_e,

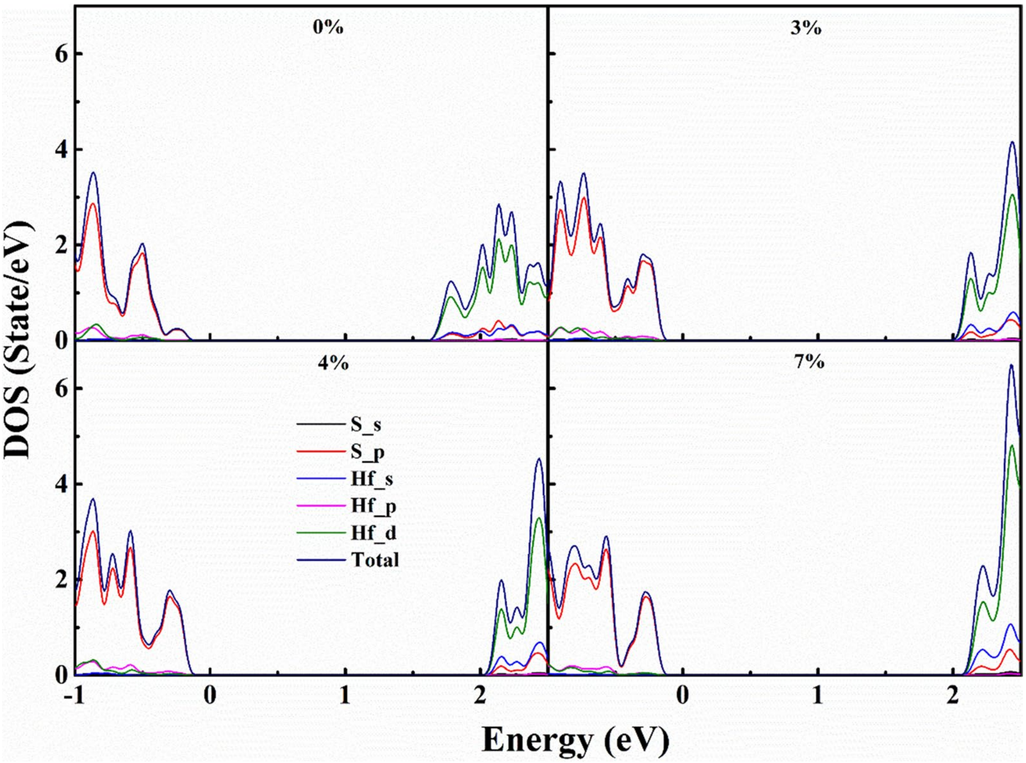

Fig. 5 The density of states of the HfS_2 bilayer at 0%, 3%, 4% and 7% strain.

Table II The effective mass (m^*), average effective mass (m_d), elastic modulus (C_{2D}), deformation potential constant (E_l), electron and hole mobility (μ) and relaxation time (τ) of HfS_2 bilayer at 0%, 1%, 2%, 3%, 4%, 5%, 6% and 7% biaxial strain

Carrier type	HfS_2-b (%)	m^* (M-Γ)	m^* (M–K)	m_d (m_0)	C_{2D} (N/m)	E_l (eV)	μ (cm^{-2} V^{-1} s^{-1})	τ (10^{-13} s)
Electrons	0	2.224	0.286	0.8	230.35	2.725	1034.3	4.71
	1	2.43	0.3	0.85	254.15	2.85	920.4	4.45
	2	2.679	0.314	0.92	206.37	2.6	769.6	4.03
	3	2.995	0.329	0.99	197.87	2.225	870.2	4.90
	4	3.429	0.346	1.09	188.46	2.55	520.5	3.23
	5	4.054	0.364	1.21	178.1	3.7	189.6	1.31
	6	4.169	0.351	1.21	168.83	3.55	195.2	1.34
	7	4.563	0.356	1.27	159.7	4	132	0.96
		m^* (Γ-M)	m^* (Γ-K)					
Holes	0	0.525	0.47	0.5	230.35	3.875	1309.4	3.73
	1	0.535	0.486	0.51	254.15	3.575	1624.8	4.72
	2	0.545	0.519	0.53	206.37	3.4	1356.1	4.09
		m^* (A-Γ)	m^* (A-K)					
	3	1.579	0.808	1.13	197.87	2.8	421.8	2.71
	4	1.569	0.797	1.12	188.46	2.95	368.4	2.35
	5	1.43	0.813	1.08	178.1	2.975	368.1	2.26
	6	1.49	0.809	1.1	168.83	2.725	400.9	2.51
	7	1.568	0.821	1.13	159.7	3.025	291.6	1.88

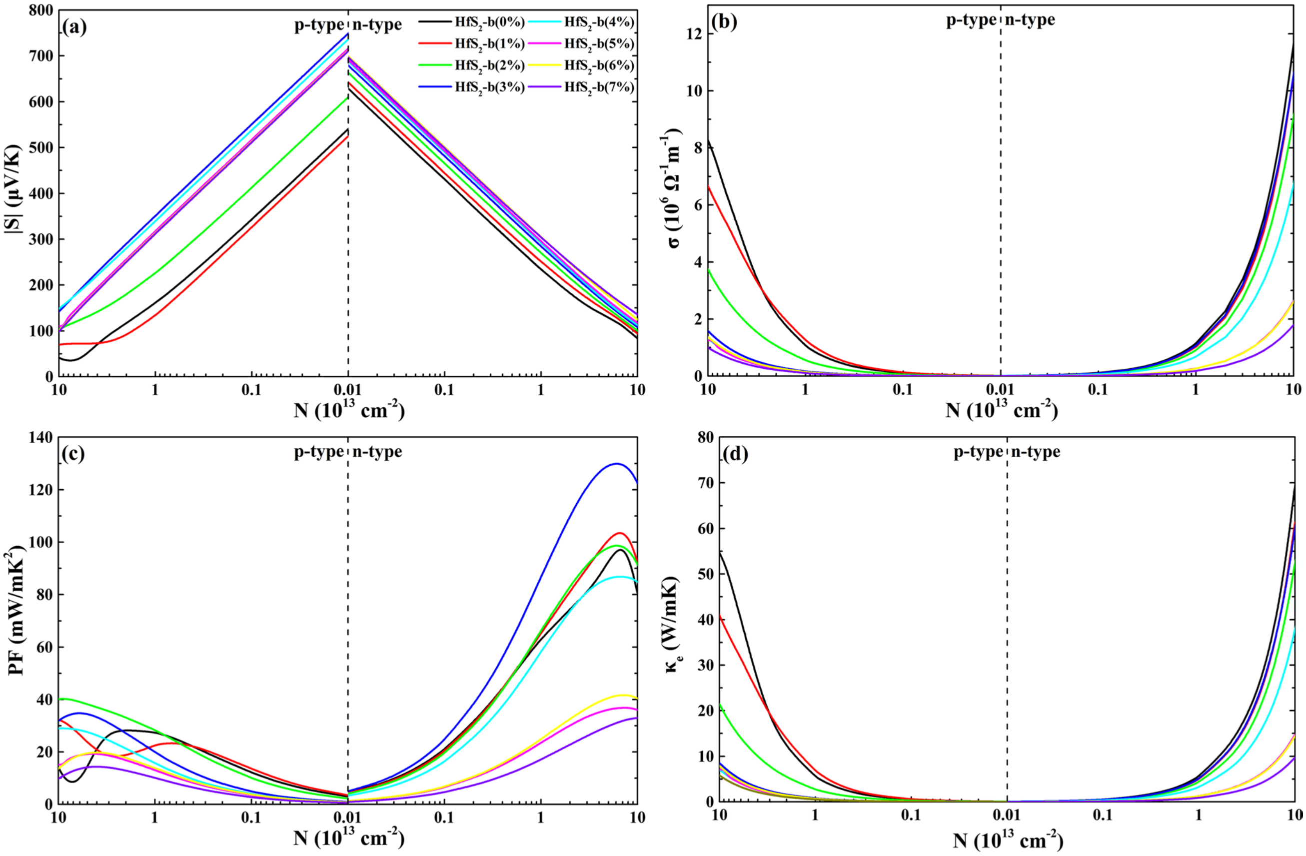

Fig. 6 The calculated electronic transport coefficients ((a) S, (b) σ, (c) PF, and (d) κ_e) as a function of carrier concentration for both p-type and n-type HfS_2 bilayers at different biaxial strain.

we obtained L under different doping concentrations through Eq. 4 as shown in Tables III and IV. Then, the variation function of κ_e with doping concentration can be obtained according to Eq. 3, as show in Fig. 6d. We can find that the variation trend of κ_e under different strains is basically consistent with the variation trend of σ.

Next, the phonon transport properties at different strains are calculated. The lattice thermal conductivity (κ_l) of HfS_2 bilayer under different strains as a function of temperature is show in Fig. 7. The κ_l not only decreases with the increase of temperature but also decreases gradually as the increase of strain. Note that we investigated the convergence of lattice thermal conductivity and the nearest neighbor number and discovered that employing three nearest neighbors is enough to get the lattice thermal conductivity to converge, as shown in Supplementary Material Fig. S2, which shows the accuracy of the calculation findings. Figure 2 shows the phonon dispersion curves under different strains, and it can be found that the acoustic branch splits at the Γ point, which is a phenomenon that does not exist in the phonon dispersion curves of the HfS_2 monolayer. The reason for this phenomenon is that the phonon scattering is affected by the interlayer force, which leads to a wider phonon scattering and reduces κ_l. Meanwhile, it can be found that the frequencies of both the acoustic branch and the optical branch gradually decrease with the strain. A lower phonon frequency often means a lower phonon group velocity, which may result in a smaller κ_l.[44] The phonon group velocity and phonon lifetime as a function of phonon frequency are given in Figs. 8 and 9 at 0%, 3%, 4% and 7% strain, respectively. Figure 8 shows that the phonon group velocities of both the acoustic and optical branches gradually decrease with strain. At 7% strain, the phonon group velocity of the acoustic branch is significantly reduced in the low-frequency region, which indicates that the phonon transmission is suppressed. It can be seen from Fig. 9 that the phonon lifetime, especially the phonon lifetime of the acoustic branch phonon is gradually decreasing with the increasing strain. The progressive enhancement

Table III Lorentz constants of the p-type HfS_2 bilayer at different biaxial strain

p-type (10^{13} cm^{-2})	HfS_2-b (0%)	HfS_2-b (1%)	HfS_2-b (2%)	HfS_2-b (3%)	HfS_2-b (4%)	HfS_2-b (5%)	HfS_2-b (6%)	HfS_2-b (7%)
0.01	1.51	1.51	1.51	1.50	1.50	1.50	1.50	1.50
0.02	1.52	1.52	1.51	1.50	1.50	1.50	1.50	1.50
0.03	1.52	1.52	1.51	1.50	1.50	1.50	1.51	1.50
0.04	1.53	1.53	1.51	1.50	1.50	1.51	1.51	1.51
0.05	1.53	1.54	1.52	1.51	1.51	1.51	1.51	1.51
0.06	1.54	1.54	1.52	1.51	1.51	1.51	1.51	1.51
0.07	1.54	1.55	1.52	1.51	1.51	1.51	1.51	1.51
0.08	1.54	1.55	1.52	1.51	1.51	1.51	1.51	1.51
0.09	1.55	1.56	1.53	1.51	1.51	1.51	1.51	1.51
0.1	1.55	1.56	1.53	1.51	1.51	1.51	1.51	1.51
0.2	1.59	1.60	1.55	1.51	1.52	1.52	1.52	1.52
0.3	1.62	1.64	1.56	1.52	1.52	1.53	1.53	1.53
0.4	1.64	1.66	1.58	1.52	1.53	1.53	1.53	1.53
0.5	1.66	1.70	1.59	1.53	1.53	1.54	1.54	1.54
0.6	1.68	1.72	1.60	1.53	1.54	1.54	1.55	1.55
0.7	1.70	1.75	1.61	1.54	1.54	1.55	1.55	1.55
0.8	1.72	1.77	1.62	1.54	1.55	1.55	1.56	1.56
0.9	1.74	1.79	1.63	1.55	1.55	1.56	1.56	1.56
1	1.75	1.82	1.64	1.55	1.55	1.57	1.57	1.57
2	1.87	1.96	1.72	1.58	1.59	1.61	1.62	1.62
3	1.95	2.02	1.76	1.61	1.62	1.65	1.65	1.66
4	2.05	2.04	1.80	1.64	1.65	1.69	1.70	1.70
5	2.14	2.04	1.82	1.67	1.68	1.72	1.74	1.74
6	2.21	2.04	1.84	1.70	1.70	1.76	1.78	1.78
7	2.24	2.04	1.86	1.72	1.72	1.80	1.81	1.82
8	2.24	2.04	1.88	1.75	1.74	1.83	1.85	1.86
9	2.23	2.04	1.90	1.77	1.76	1.89	1.89	1.89
10	2.20	2.05	1.91	1.80	1.78	1.89	1.93	1.93

Table IV Lorentz constants of the n-type HfS_2 bilayer at different biaxial strain

n-type (10^{13} cm^{-2})	HfS_2-b (0%)	HfS_2-b (1%)	HfS_2-b (2%)	HfS_2-b (3%)	HfS_2-b (4%)	HfS_2-b (5%)	HfS_2-b (6%)	HfS_2-b (7%)
0.01	1.50	1.50	1.50	1.50	1.50	1.50	1.50	1.50
0.02	1.51	1.51	1.51	1.50	1.50	1.50	1.50	1.50
0.03	1.51	1.51	1.51	1.51	1.51	1.51	1.51	1.51
0.04	1.51	1.51	1.51	1.51	1.51	1.51	1.51	1.51
0.05	1.51	1.51	1.51	1.51	1.51	1.51	1.51	1.51
0.06	1.52	1.51	1.51	1.51	1.51	1.51	1.51	1.51
0.07	1.52	1.52	1.51	1.51	1.51	1.51	1.51	1.51
0.08	1.52	1.52	1.52	1.51	1.51	1.51	1.51	1.51
0.09	1.52	1.52	1.52	1.51	1.51	1.51	1.51	1.51
0.1	1.52	1.52	1.52	1.52	1.51	1.51	1.51	1.51
0.2	1.54	1.54	1.53	1.53	1.52	1.52	1.52	1.52
0.3	1.55	1.55	1.54	1.54	1.53	1.53	1.53	1.53
0.4	1.57	1.56	1.55	1.54	1.54	1.54	1.54	1.54
0.5	1.58	1.57	1.56	1.55	1.55	1.55	1.54	1.54
0.6	1.59	1.58	1.57	1.56	1.56	1.55	1.55	1.55
0.7	1.60	1.59	1.57	1.57	1.56	1.56	1.56	1.56
0.8	1.61	1.60	1.58	1.57	1.57	1.57	1.56	1.56
0.9	1.63	1.61	1.59	1.58	1.58	1.57	1.57	1.57
1	1.63	1.62	1.60	1.59	1.58	1.58	1.57	1.57
2	1.71	1.68	1.66	1.64	1.63	1.63	1.62	1.62
3	1.76	1.73	1.70	1.69	1.68	1.67	1.66	1.65
4	1.80	1.77	1.74	1.73	1.72	1.71	1.69	1.68
5	1.83	1.80	1.78	1.76	1.75	1.74	1.72	1.71
6	1.86	1.83	1.81	1.79	1.78	1.77	1.74	1.73
7	1.89	1.86	1.84	1.82	1.81	1.80	1.77	1.76
8	1.92	1.89	1.87	1.85	1.84	1.82	1.80	1.78
9	1.95	1.92	1.90	1.87	1.86	1.84	1.82	1.79
10	1.99	1.95	1.92	1.90	1.88	1.87	1.85	1.81

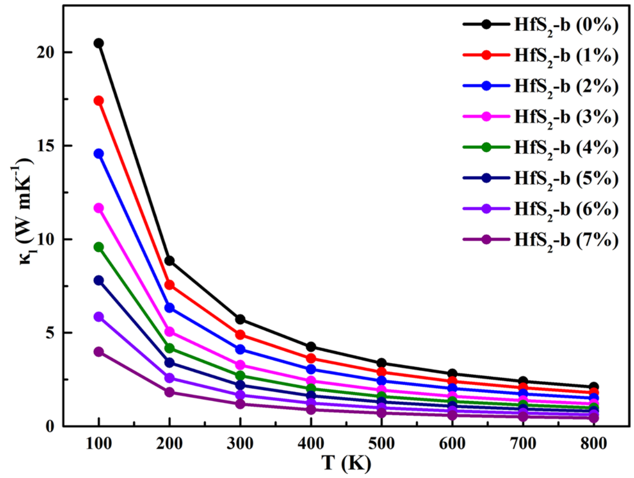

Fig. 7 The calculated lattice thermal conductivity of HfS_2 bilayer as a function of temperature at different biaxial strain.

of phonon scattering and the shortening of phonon lifetime also tend to imply a smaller κ_l.

Combining the obtained electronic thermal conductivities and lattice thermal conductivities, we obtain κ as a function of doping concentration for different strains at 300 K, as shown in Fig. 10. We can see from Fig. 10 that κ is decreasing with strain.

Figure of Merit *ZT*

Combining the obtained PF and κ, $ZT = S^2\sigma T/\left(\kappa_e + \kappa_l\right)$ as a function of doping concentration under different strains at a temperature of 300 K is finally obtained, as shown in Fig. 11. For the *p*-type HfS_2 bilayer, the PF is relatively high when the strain is small, but the *ZT* value is relatively high when the strain is large. This is because the *PF* changes very little under different strains, but at 6% and 7% strain, κ decreases greatly, resulting in an increase in *ZT*. At 6% strain, the maximum *ZT* value is 1.83, the *PF* is 13.81 mW/mK^2 and

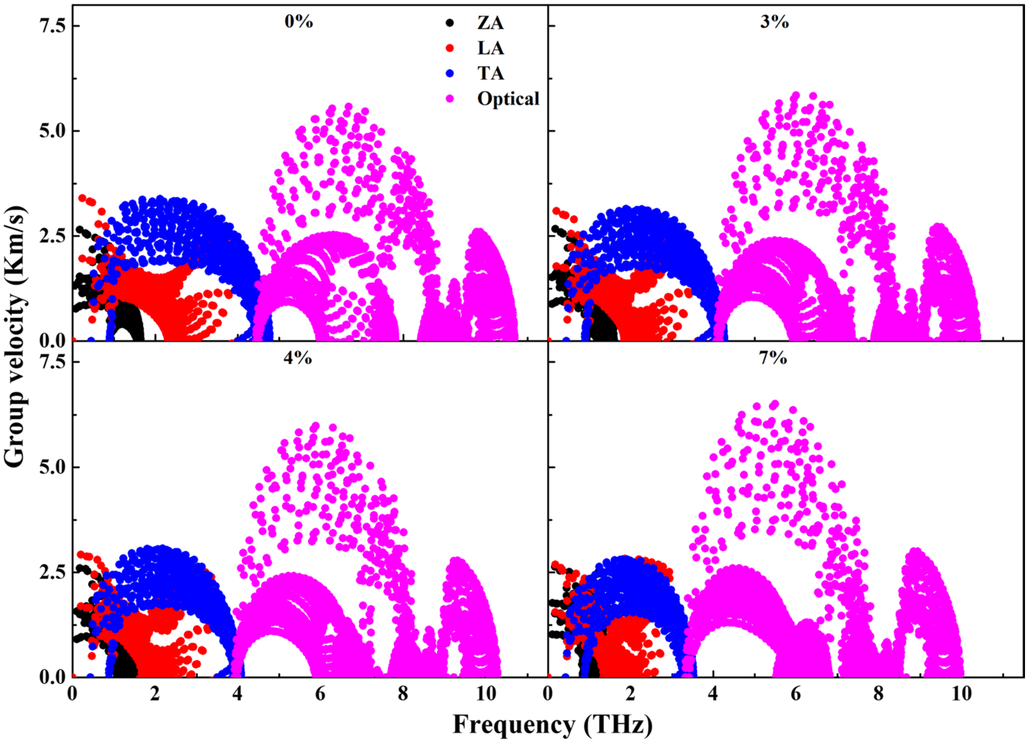

Fig. 8 Magnitude of phonon group velocity as a function of frequency in the full BZ under 0%, 3%, 4% and 7% biaxial strain.

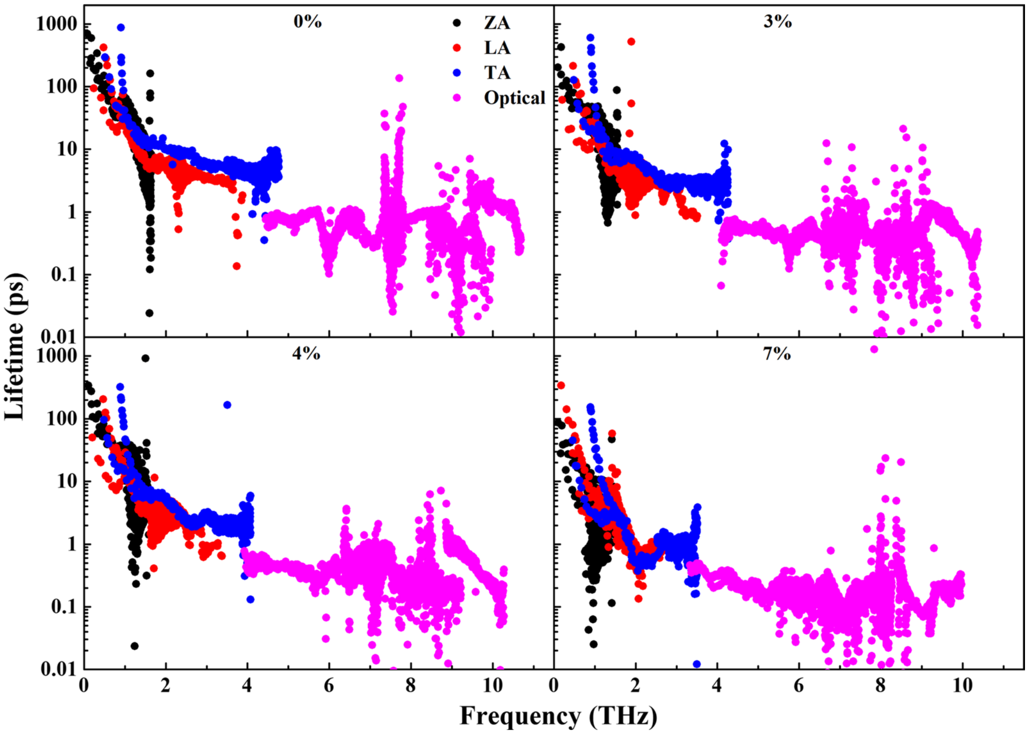

Fig. 9 Mode-dependent phonon relaxation times as a function of frequency in the full BZ under 0%, 3%, 4% and 7% biaxial strain.

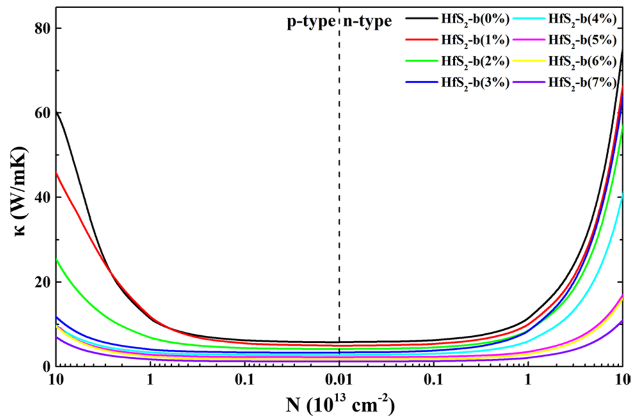

Fig. 10 The calculated total thermal conductivity of HfS_2 bilayer as a function of carrier concentration at different biaxial strain.

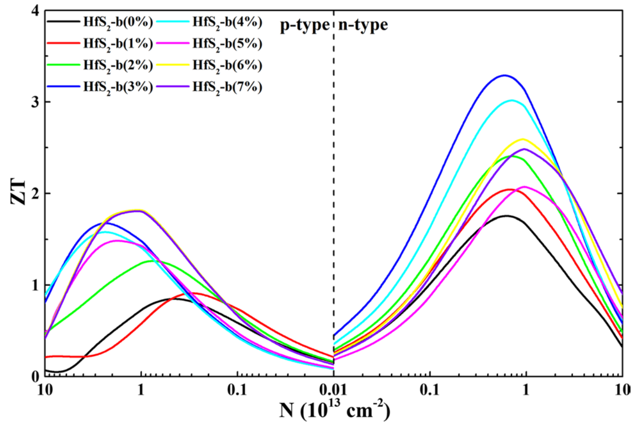

Fig. 11 The calculated *ZT* as a function of carrier concentration for both *p*-type and *n*-type bilayer HfS_2 at different biaxial strain.

κ is 2.27 W/mK at a hole concentration of 1×10^{13} cm^{-2}. Conversely, for *n*-type doping, the *PF* is 69.87 mW/mK^2, κ is 6.36 W/mK and the maximum *ZT* value is 3.29 at 3% strain and electron concentration of 6×10^{12} cm^{-2}. Although the κ of *n*-type doping is much higher than that of *p*-type at the optimal doping concentration, the *PF* is much higher than that of *p*-type. Moreover, the *PF* of *n*-type doping at 3% strain is much higher than that under other strains, which means that the main factor affecting the change of *ZT* value is *PF* rather than κ. For *p*-type doping, the opposite is true. Because the *PF* is not much different, the main factor affecting the *ZT* value is κ.

The thermoelectric performance of the HfS_2 bilayer is higher compared with the HfS_2 monolayer. For example, Bera et al. calculated a maximum *ZT* value of 0.60 for the HfS_2 monolayer and Özbal et al. reported a maximum *ZT* value of 0.67.[26,38] According to the research in this paper, the maximum *ZT* value of the unstrained HfS_2 bilayer is 1.76, which is larger than the *ZT* value of the HfS_2 monolayer.

Conclusion

In this chapter, the band structure, electronic transport properties and thermal transport properties of HfS_2 bilayer under different biaxial strains are calculated based on first principles combined with Boltzmann equation and the thermoelectric properties are obtained finally. For the unstrained HfS_2 bilayer, the maximum *ZT* value of *p*-type doping is 0.85, while the maximum *ZT* value of *n*-type is 1.76, which indicates that the bilayer structure can effectively improve the thermoelectric properties of 2D HfS_2. The degenerate bands and stair-like 2D DOS contribute to the high *PF*, while the interlayer force leads to enhanced phonon scattering and reduces the κ_l, which improves the *ZT* value of the HfS_2 bilayer.

By applying biaxial tensile strain to the HfS_2 bilayer, it is found that the strain induces a change in the band structure and increases the degeneracy of the band, thereby improving the *PF* of the material. Meanwhile, the κ_l of HfS_2 bilayer can be greatly reduced with the strain due to the enhancement of phonon scattering and the decrease of phonon lifetime. The thermoelectric performance of HfS_2 bilayer can be greatly improved under the dual effect of the improvement of PF and the reduction of κ. Ultimately, we further enhance the thermoelectric properties of HfS_2 bilayer by strain engineering. For *p*-type doping, the *ZT* value of the HfS_2 bilayer at 6% strain is improved to 1.83; while the *ZT* value of the HfS_2 bilayer at 3% strain under the *n*-type doping is more higher, reaching 3.29.

Supplementary Information The online version contains supplementary material available at https://doi.org/10.1007/s11664-023-10443-5.

Acknowledgments The authors would like to acknowledge the National Natural Science Foundation of China Nos. 11504304, 11972313, The Funded by the Project of State Key Laboratory of Environment-friendly Energy Materials, Southwest University of Science and Technology No. 19fksy0007, No. 20fksy0023. Moreover, thanks to Dr. Lei Liu (Southwest University of Science and Technology, Mianyang, Sichuan 610064, China) for your guidance.

Conflict of interest The authors declare that they have no conflict of interest.

References

1. S. Manzeli, D. Ovchinnikov, D. Pasquier, O.V. Yazyev, and A. Kis, 2D transition metal dichalcogenides. *Nat. Rev. Mater.* 2, 17033 (2017).

2. D. Wang, X. Zhang, and Z. Wang, Recent advances in properties, synthesis and applications of two-dimensional HfS_2. *J. Nanosci. Nanotechnol.* 18, 7319 (2018).
3. D. Li, Y. Gong, Y. Chen, J. Lin, Q. Khan, Y. Zhang, Y. Li, H. Zhang, and H. Xie, Recent progress of two-dimensional thermoelectric materials. *Nano-Micro Lett.* 12, 36 (2020).
4. M. Faghihnasiri, A. Ahmadi, S.A. Golpayegan, S.G. Sharifabadi, and A. Ramazani, A first-principles study of nonlinear elastic behavior and anisotropic electronic properties of two-dimensional HfS_2. *Nanomaterials* 10, 446 (2020).
5. J. Shang, L. Huang, and Z. Wei, Effects of vertical electric field and compressive strain on electronic properties. *J. Semicond.* 38, 033001 (2017).
6. Q. Zhao, Y. Guo, K. Si, Z. Ren, J. Bai, and X. Xu, Elastic, electronic, and dielectric properties of bulk and monolayer ZrS_2, $ZrSe_2$, HfS_2, $HfSe_2$ from van der Waals density-functional theory. *Phys. Status. Solidi. B.* 254, 1700033 (2017).
7. G. Ding, G.Y. Gao, Z. Huang, W. Zhang, and K. Yao, Thermoelectric properties of monolayer MSe_2 (M = Zr, Hf): low lattice thermal conductivity and a promising figure of merit. *Nanotechnology* 27, 375703 (2016).
8. S. Kumar and U. Schwingenschlögl, Thermoelectric response of bulk and monolayer $MoSe_2$ and WSe_2. *Chem. Mater.* 27, 1278 (2015).
9. G. Yumnam, T. Pandey, and A.K. Singh, High temperature thermoelectric properties of Zr and Hf based transition metal dichalcogenides: a first principles study. *J. Chem. Phys.* 143, 234704 (2015).
10. H.Y. Lv, W.J. Lu, D.F. Shao, H.Y. Lu, and Y.P. Sun, Strain-induced enhancement of thermoelectric performance in a ZrS_2 monolayer. *J. Mater. Chem. C.* 4, 4538 (2016).
11. Z. Jin, Q. Liao, H. Fang, Z. Liu, W. Liu, Z. Ding, T. Luo, and N. Yang, A revisit to high thermoelectric performance of single-layer MoS_2. *Sci. Rep.* 5, 18342 (2015).
12. D. Wickramaratne, F. Zahid, and R.K. Lake, Electronic and thermoelectric properties of few-layer transition metal dichalcogenides. *J. Chem. Phys.* 140, 124710 (2014).
13. A.A. Ramanathan and J.M. Khalifeh, Enhanced thermoelectric properties of suspended mono- and bilayer of MoS_2 from first principles. *IEEE Trans. Nanotechnol.* 17, 974 (2018).
14. Y. Sun, H. Cheng, S. Gao, Q. Liu, Z. Sun, C. Xiao, C. Wu, S. Wei, and Y. Xie, Atomically thick bismuth selenide freestanding single layers achieving enhanced thermoelectric energy harvesting. *J. Am. Chem. Soc.* 134, 20294 (2012).
15. V. Goyal, D. Teweldebrhan, and A. Balandin, Mechanically-exfoliated stacks of thin films of Bi_2Te_3 topological insulators with enhanced thermoelectric performance. *Appl. Phys. Lett.* 97, 133117 (2010).
16. Z.Z. Zhou, H.J. Liu, D.D. Fan, G.H. Cao, and C.Y. Sheng, High thermoelectric performance in the hexagonal bilayer structure consisting of light boron and phosphorus elements. *Phys. Rev. B* 99, 085410 (2019).
17. J. Tseng and X. Luo, First-principles investigation of low-dimension MSe_2 (M = Ti, Hf, Zr) configurations as promising thermoelectric materials. *J. Phys. Chem. Solids.* 139, 109322 (2020).
18. D. Qin, X.J. Ge, G.Q. Ding, G.Y. Gao, and J.T. Lv, Strain-induced thermoelectric performance enhancement of monolayer $ZrSe_2$. *RSC Adv.* 7, 47243 (2017).
19. M.K. Mohanta, A. Rawat, N. Jena, R. Ahammed, and A.D. Sarkar, Superhigh flexibility and out-of-plane piezoelectricity together with strong anharmonic phonon scattering induced extremely low lattice thermal conductivity in hexagonal buckled CdX (X = S, Se) monolayers. *J. Phys. Condens. Matter.* 32, 355301 (2020).
20. G. Ozbal, R.T. Senger, C. Sevik, and H. Devincil, Ballistic thermoelectric properties of monolayer semiconducting transition metal dichalcogenides and oxides. *Phys. Rev. B Condens. Mater. Mater. Phys.* 100, 085415 (2019).
21. S.D. Guo and Y.H. Wang, Thermoelectric properties of orthorhombic group IV–VI monolayers from the first-principles calculations. *J. Appl. Phys.* 121, 034302 (2017).
22. C. Yan, C. Gong, P. Wangyang, J. Chu, K. Hu, C. Li, X. Wang, X. Du, T. Zhai, Y. Li, and J. Xiong, 2D group IVB transition metal dichalcogenides. *Adv. Funct. Mater.* 28, 1803305 (2018).
23. W.X. Zhang, Z.S. Huang, W.L. Zhang, and Y.R. Li, Two-dimensional semiconductors with possible high room temperature mobility. *Nano Res.* 7, 1731 (2014).
24. M. Abdulsalam, E. Rugut, and D.P. Joubert, Mechanical, thermal and thermoelectric properties of MX_2 (M = Zr, Hf; X = S, Se). *Mater. Today Commun.* 25, 101434 (2020).
25. G. Kresse and F. Hafner, Ab Initio molecular dynamics for liquid metals. *Phys. Rev. B: Condens. Matter.* 47, 558 (1993).
26. G. Kresse and D. Joubert, From ultrasoft pseudopotentials to the projector augmented-wave method. *Phys. Rev. B: Condens. Matter.* 59, 1758 (1999).
27. J.P. Perdew, K. Burke, and M. Ernzerhof, Ceramic expansion by water layers on magnesium oxide: AB initio study. *Phys. Rev. Lett.* 77, 3865 (1996).
28. S. Grimme, Semiempirical GGA-type density functional constructed with a long-range dispersion correction. *J. Comput. Chem.* 27, 1787 (2006).
29. A. Kandemir and H. Sahin, Bilayer of janus WSSe: monitoring the stacking type via vibrational spectrum. *Phys. Chem. Chem. Phys.* 20, 17380 (2018).
30. G.K.H. Madsen and D.J. Singh, BoltzTraP. A code for calculating band-structure dependent quantities. *Comput. Phys. Commun.* 175, 67 (2006).
31. S.I. Takagi, A. Toriumi, M. Iwase, and H. Tango, On the universality of inversion layer mobility in Si MOSFET's: Part I-effects of substrate impurity concentration. *IEEE Trans. Electron Dev.* 41, 2357 (1994).
32. H.S. Kim, Z.M. Gibbs, Y. Tang, H. Wang, and G.J. Snyder, Characterization of Lorenz number with seebeck coefficient measurement. *APL. Mater.* 3, 041506 (2015).
33. W. Li, W. Carrete, N.A. Katcho, and N. Mingo, ShengBTE: a solver of the Boltzmann transport equation for phonos. *Comput. Phys. Commun.* 185, 1747 (2014).
34. A. Togo, F. Oba, and I. Tanaka, First-Principles calculations of the ferroelastic transition between rutile-type and $CaCl_2$-type SiO_2 at high pressure. *Phys. Rev. B.* 78, 134106 (2008).
35. X. Chen, D. Wang, X. Liu, L. Li, and B. Sanyal, Two-dimensional square-A_2B (A =Cu, Ag, Au, and B= S, Se): auxetic semiconductors with high carrier mobilities and unusually low lattice thermal conductivities. *J. Phys. Chem. Lett.* 11, 2925 (2020).
36. S.S. Batsanov, Van der Waals Radii of elements. *Inorg. Mater.* 37, 871 (2001).
37. J. Bera, A. Betal, and S. Sahu, Spin orbit coupling induced enhancement of thermoelectric performance of HfX_2 (X = S, Se) and its Janus monolayer. *J. Alloys. Compd.* 872, 159704 (2021).
38. D.T. Hodul and A.M. Stacy, Anomalies in the properties of $Hf(S_{2\text{-}x}Te_x)_{1\text{-}y}$ and $Hf(Se_{2\text{-}x}Te_x)_{1\text{-}y}$ near the metal-insulator transition. *J. Solid. State. Chem.* 543, 438 (1984).
39. G. Tan, L.D. Zhao, and M.G. Kanatzidis, Rationally designing high-performance bulk thermoelectric materials. *Chem. Rev.* 116, 12123 (2016).
40. Y. Pei, H. Wang, and G. Snyder, Band engineering of thermoelectric materials. *Adv. Mater.* 24, 6125 (2012).
41. Y. Pei, X. Shi, A. Lalonde, H. Wang, L. Chen, and G.J. Snyder, Convergence of electronic bands for high performance bulk thermoelectrics. *Nature* 473, 66 (2011).

42. J. Bera and S. Sahu, Strain induced valley degeneracy: a route to the enhancement of thermoelectric properties of monolayer WS_2. *RSC Adv.* 9, 25216 (2019).
43. N. Wang, M. Li, H. Xiao, H. Gong, Z. Liu, X. Zu, and L. Qiao, Optimizing the thermoelectric transport properties of Bi_2O_2Se monolayer via biaxial strain. *Phys. Chem. Chem. Phys.* 21, 15097 (2019).
44. P. Yan, G.Y. Gao, G.Q. Ding, and D. Qin, Bilayer MSe_2 (M = Zr, Hf) as promising two-dimensional thermoelectric materials: a first-principles study. *RSC Adv.* 9, 12394 (2019).